

Article

Metal Oxide (Co₃O₄ and Mn₃O₄) Impregnation into S, N-doped Graphene for Oxygen Reduction Reaction (ORR)

Penny Mathumba ¹, Diana M. Fernandes ^{2,*}, Renata Matos ², Emmanuel I. Iwuoha ¹ and Cristina Freire ²

¹ Department of Chemistry, Faculty of Science, University of the Western Cape (UWC), Cape Town, Bellville 7535, South Africa; mathumbapz@gmail.com (P.M.); eiwuoha@uwc.ac.za (E.I.I.)

² REQUIMTE/LAQV, Departamento de Química e Bioquímica, Faculdade de Ciências, Universidade do Porto, 4160-007 Porto, Portugal; renata.matos@fc.up.pt (R.M.); acfreire@fc.up.pt (C.F.)

* Correspondence: diana.fernandes@fc.up.pt

Received: 2 March 2020; Accepted: 26 March 2020; Published: 28 March 2020



Abstract: To address aggravating environmental and energy problems, active, efficient, low-cost, and robust electrocatalysts (ECs) are actively pursued as substitutes for the current noble metal ECs. Therefore, in this study, we report the preparation of graphene flakes (GF) doped with S and N using 2-5-dimercapto-1,3,4-thiadiazole (S₃N₂) as precursor followed by the immobilization of cobalt spinel oxide (Co₃O₄) or manganese spinel oxide (Mn₃O₄) nanoparticles through a one-step co-precipitation procedure (Co/S₃N₂-GF and Mn/S₃N₂-GF). Characterization by different physicochemical techniques (Fourier Transform Infrared (FTIR), Raman spectroscopy, Transmission Electron Microscopy (TEM) and X-ray Diffraction (XRD)) of both composites shows the preservation of the metal oxide spinel structure and further confirms the successful preparation of the envisaged electrocatalysts. Co/S₃N₂-GF composite exhibits the best ORR performance with an onset potential of 0.91 V vs. RHE, a diffusion-limiting current density of -4.50 mA cm^{-2} and selectivity for the direct four-electron pathway, matching the results obtained for commercial Pt/C. Moreover, both Co/S₃N₂-GF and Mn/S₃N₂-GF showed excellent tolerance to methanol poisoning and good stability.

Keywords: oxygen reduction; carbon material; metal oxides; heteroatom doping

1. Introduction

The continuous exhaustion of fossil fuels highly contributing to environmental problems and the increasing demand of energy has prompted the development of sustainable alternative energy sources and conversion devices like metal–air batteries and fuel cells. The major problem for the wide spread of these new technologies is related to the fact that the reaction occurring at the cathode, the oxygen reduction reaction (ORR), has sluggish kinetics and is the major rate-limiting factor restricting achieving the expected performance [1]. Ideally, this reaction should occur through a direct four-electron process, but for most of the electrocatalysts developed it occurs through a less efficient two-electron process with the production of an intermediate—hydrogen peroxide.

Currently, the most efficient electrocatalysts for ORR are noble metal platinum (Pt)-based materials with low overpotential, large current densities and selectivity toward the direct four-electron process [2,3]. However, these are extremely expensive due to limited platinum resources on earth, and they suffer deactivation due to methanol poisoning [3]. Consequently, the development and application of fuel cells and metal–air batteries have been limited. These drawbacks have stimulated the search for alternative, cost-effective and stable ORR electrocatalysts.

Among the most promising electrocatalysts to displace the expensive Pt/C are the earth-abundant first row transition metal nitrogen-doped carbons. These have gained particular attention since 1964, when Jasinski first observed ORR activity on a cobalt macrocyclic complex [4,5]. Cobalt and manganese oxides have emerged as a promising group of non-precious metal electrocatalysts due to their intrinsic electrocatalytic activity attributed to their characteristic mixed-valence states, high stability, low environmental impact, and exceptional 3d electronic configurations [6–9]. However, the limited number of active sites and the poor electrical conductivity have limited their wide application [10]. This drawback can be circumvented by designing hybrid materials of metal oxides supported onto electrically conductive materials. Carbon materials have been proven to modulate the electrical conductivity of cobalt, for example, by providing increased charge transport and exposing active sites due to the high surface area of carbon, thereby promoting the electrocatalytic activity of cobalt [11,12]. However, some studies have reported a limitation in electron transfer at the interface and restricted electrocatalytic tunability caused by the lack of bridged bonds between the carbon lattice and metal oxide, commanding the use of doped carbon to create effective bonds [13,14]. Graphene-based transition metal oxide (Fe, Co, Cu, Ni, and Mn) nanocomposites have already been a subject of study and have been proven to be a promising type of highly efficient and economic nanocatalyst for optimizing the ORR to solve the current energy crisis [11,15]. For example, iron oxides supported on N-doped carbon catalysts have been studied for a long time for the ORR due to the extremely low cost of Fe and their good performance in both acidic and alkaline electrolytes [16]. Similarly, different researchers reported the synthesis of cobalt oxides/N-graphene for ORR with very good electrocatalytic performances [17].

With this in mind, here we report the preparation of graphene flakes doped with nitrogen and sulfur (S_3N_2 -GF) to serve as bridging atoms to facilitate electron transport. Subsequently, two composites based on the immobilization of Co_3O_4 and Mn_3O_4 nanoparticles supported on S_3N_2 -GF were developed and efficiently employed for oxygen reduction. A scalable and easy procedure was used for the N- and S-doping process which constitutes an advantage. Additionally, the designed ECs exhibited enhanced ORR performances as a result of the covalent coupling effect between the S- and N-doped GF and the metal oxide nanoparticles.

2. Materials and Methods

2.1. Materials and Instrumentation

The materials and solvents used in the electrocatalyst preparation and in the electrocatalytical studies were used as received and are described in detail in the Supplementary Material (SM) file. All electrocatalysts were characterized prior to their application using different techniques (Raman, FT-IR, XRD, XPS and TEM) and the methods and equipment used are detailed in the SM file.

Electrocatalytic performance was evaluated using a PGSTAT 302N potentiostat (Metrohm Autolab B.V., Utrecht, The Netherlands) controlled by NOVA 2.1 and using a conventional 3-electrode system. For all details regarding electrodes, electrode conditioning and modification, see the SM file.

2.2. Synthesis of S, N-graphene Flakes (S_3N_2 -GF)

The preparation of dual-doped GF (nitrogen and sulfur) was achieved using a precursor containing both heteroatoms (2-5-dimercapto-1,3,4-thiadiazole, S_3N_2). Briefly, 400 mg of GF was mixed with 400 mg of S_3N_2 in a ball miller (Retsch MM200, Retsch GMBH, Haan, Germany) at 15 Hz for 5 hours. For a proper mixing of the two components, were chosen balls of zirconium oxide with a 2 mm diameter (≈ 100). Then, the mixture was subjected to calcination at 800 °C for 1 hour under N_2 flow.

2.3. Synthesis of Co and Mn/ S_3N_2 -GF

For Co/ S_3N_2 -GF, the S, prior-prepared N-doped GF (235 mg) were dispersed in aqueous solution (50 mL) containing 4 mmol of $CoCl_2 \cdot 6H_2O$. Then, the solution of 1-amino-2-propanol (MIPA) (3 mol dm^{-3}) was added, at a rate of 50 mL h^{-1} , until the pH = 10. This mixture was stirred at room

temperature during 24 h and the slurry material was filtered, washed with water and ethanol and left to dry 12 h under vacuum (at 50 °C). Finally, the obtained material was calcined at 250 °C for 3 h in air. For the preparation of Mn/S₃N₂-GF, the procedure was very similar: 217 mg of S₃N₂-GF and 4.4 mmol MnCl₂·4H₂O were used, and calcination with air flux for 5 h at 300 °C.

3. Results and Discussion

3.1. Electrocatalysts Characterization

The successful doping of graphene flakes was confirmed by X-ray photoelectron spectroscopy (XPS) analysis and the high-resolution spectra are depicted in Figure S1. The C 1s high-resolution spectrum of S₃N₂-GF was fitted with six peaks at: 283.0 (C–S–C), 284.6 eV (sp², C–C, C=C), 286.1 eV (C–O, C–N), 287.1 eV (C=O), 288.3 eV (O–C=O), and 290.7 eV (π–π* transition) [18,19]. The fitting was similar to that of pristine GF published previously with the exception of a new small peak corresponding to C–S–C (from doping with S₃N₂) and the contribution of C–N bonds to the peak at 286.1 eV [18]. The O 1s high-resolution spectrum of S₃N₂-GF is shown in Figure S1b and was fitted with three peaks: one at ≈ 531.3 eV corresponding to C=O, one at ≈ 532.8 eV attributed to C–O and another at ≈ 534.6 eV assigned to O–C=O [18,20]. The N 1s XPS spectrum of S₃N₂-GF (Figure S1c) was fitted with three main peaks at 398.4, 399.8 and 400.7 eV, attributed to pyridiniC–N, pyrroliC–N, and graphitic N, respectively. Those at 398.4 and 399.8 eV may be attributed to the π-conjugated system with a pair of p-electrons in graphene layers, while those at 400.7 eV demonstrate the replacement of N atoms in the carbon layers [21,22]. The S 2p XPS spectrum (Figure S1d) is slightly complex due to spin-orbital coupling phenomenon. The pair of peaks at ≈ 163.9 eV (2p_{3/2}) and 164.9 eV (2p_{1/2}) can be attributed to the C–S–C covalent bonds, those at 165.4 and 166.4 eV to C–SH, and that at 168.6 eV is assigned to some oxidized sulphur (–C–SO_x–C–, x = 2, 3) [23,24]. The XPS surface atomic percentages were also determined, at 97.1% (C 1s), 1.1% (O 1s), 1.1% (N 1s) and 0.5% (S 2p).

The initial assessment of the composite ECs was performed by FTIR and the spectra of Co/S₃N₂-GF and Mn/S₃N₂-GF are exhibited in Figure 1 (see Figure S2 for full spectra). For comparison, those of metal oxide NPs are also included. The presence of two bands at 575 and 662 cm^{−1} in the Co/S₃N₂-GF spectrum (Figure 1a) confirms the successful preparation of the desired composite. These two bands confirm the Co₃O₄ with spinel structure [25,26]. Similarly, the presence of two bands at 629 and 522 cm^{−1} in the Mn/S₃N₂-GF spectrum (Figure 1b) indicates that the Mn₃O₄ nanoparticles were prepared with spinel structure [21,27]. The composites also present the bands related to the S, N-doped GF (≈3591, 1534, 1325 and 1178 cm^{−1}). Those at approximately 3591, 1534 and 1178 cm^{−1} correspond to the stretching vibrations of the OH groups, C=C and C–O/ C–S, respectively, while that at 1325 cm^{−1} corresponds to the C–N stretching vibration [28,29].

Raman spectra of the prepared composites and of S₃N₂-GF, Co₃O₄ and Mn₃O₄ nanoparticles are depicted in Figure 2. The spectrum of the S₃N₂-GF shows peaks at 1336 cm^{−1} (D band), 1570 cm^{−1} (G band), 2684 cm^{−1} (2D band) and a smaller one at 2926 cm^{−1} (D + G band). Graphene doping shifts the Fermi level away from the Dirac point, decreasing the probability of charge carrier recombination [30]. The reduced recombination increases and sharpens the G band as can be seen in Figure 2. An increased electron (e[−]) concentration results in a decrease in the 2D band peak position, with an expanded crystal lattice, decreased Raman phonons and asymmetry in the doping effect of the G band peak position [31,32]. The presence of Co₃O₄ nanoparticles in the Co/S₃N₂-GF composite (Figure 2a) is confirmed by the peaks assigned to the Raman active modes of the Co₃O₄ structure at 671 (A_{1g}), 603 (F_{2g}), 507 (F_{2g}) and 466 cm^{−1} (E_g) [33,34]. The presence of the Raman bands corresponding to the doped carbon material is also observed (1342, 1573 and 2694 cm^{−1}). The slight shift in the peak positions with respect to the undoped material suggests the interaction between the doped GF and the nanoparticles.

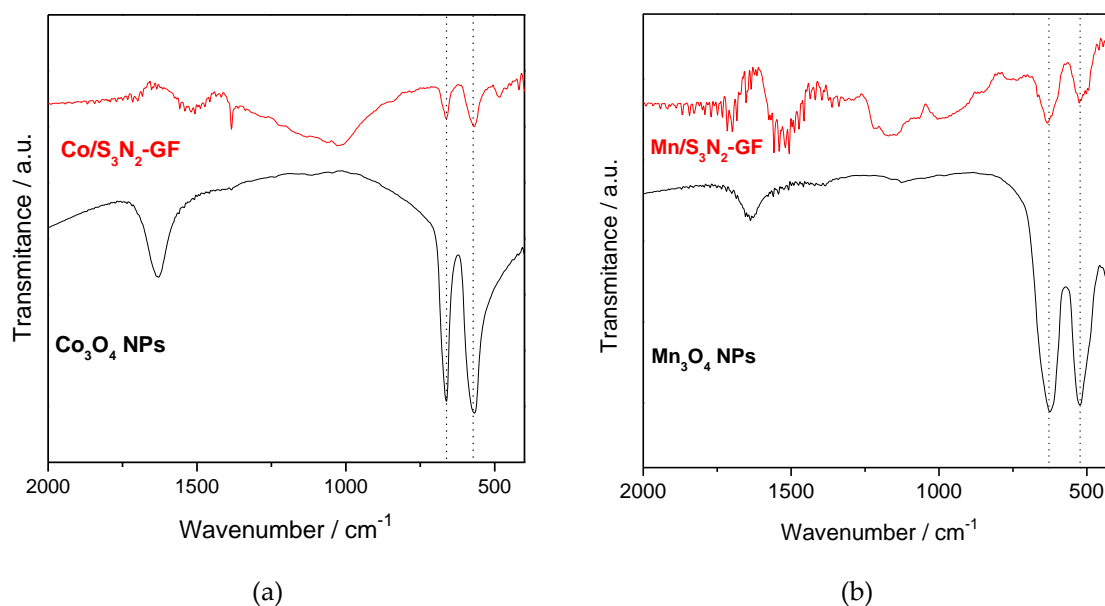


Figure 1. FTIR spectra of $\text{Co/S}_3\text{N}_2\text{-GF}$ (a) and $\text{Mn/S}_3\text{N}_2\text{-GF}$ (b) composites.

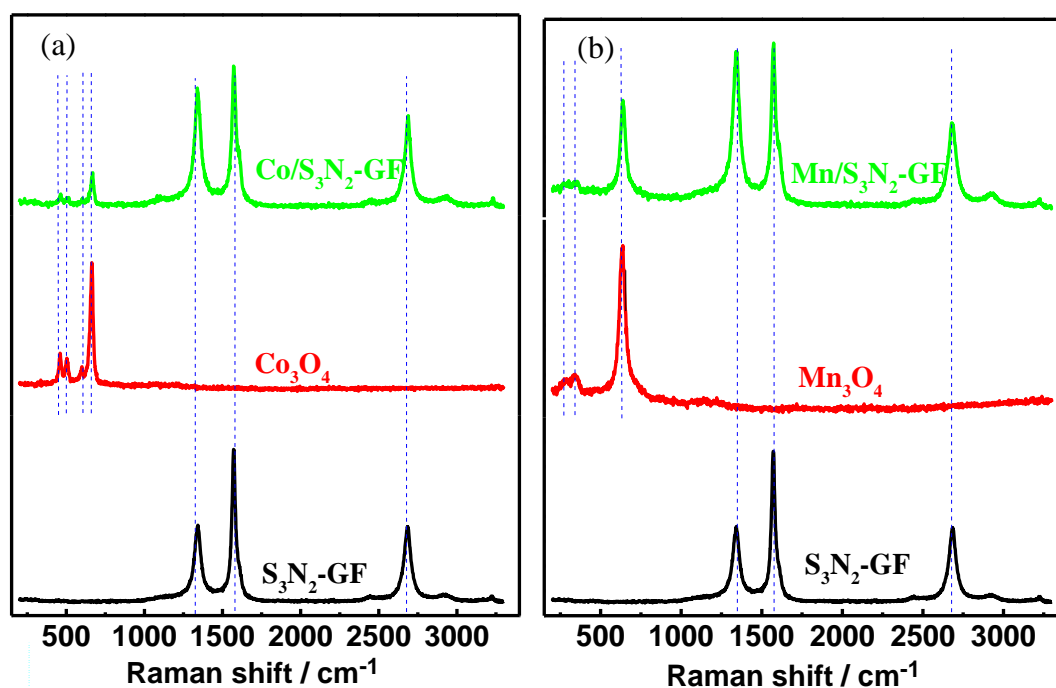


Figure 2. Raman spectra of $\text{Co/S}_3\text{N}_2\text{-GF}$ (a) and $\text{Mn/S}_3\text{N}_2\text{-GF}$ (b) composites.

The successful in situ preparation of Mn_3O_4 nanoparticles with spinel structure in the presence of $\text{S}_3\text{N}_2\text{-GF}$ (Figure 2b) is also confirmed through the existence of Raman peaks at 640 (A_{1g}), 351 (T_{2g}) and 273 cm^{-1} (E_g). The peaks assigned to the D, G and 2D modes are also observed at 1342 cm^{-1} , 1575 cm^{-1} and 2682 cm^{-1} , respectively.

XRD analysis was also carried out and the patterns can be observed in Figure 3. The XRD pattern of $\text{S}_3\text{N}_2\text{-GF}$ shows diffraction peaks at 25° , 43° and 54° , corresponding to the 002, 100 and 101 XRD crystal planes, respectively, which can be indexed to the hexagonal crystalline graphite (JCPDS No. 41-1487) [35,36]. The XRD pattern of Co_3O_4 NPs (Figure 3a) shows the typical diffraction peaks indexed to the (111), (220), (311), (222), (400), (511) and (440) crystal planes of face-centred-cubic phase

of the Co_3O_4 spinel structure at $2\theta = 19^\circ, 31^\circ, 37^\circ, 38^\circ, 45^\circ, 59^\circ$ and 65° (JCPDS No. 42-1467) [37]. These results are in accordance with previously reported results [21,37,38]. The $\text{Co}/\text{S}_3\text{N}_2\text{-GF}$ XRD patterns present one peak at $2\theta = 26^\circ$ assigned to the (002) XRD plane of stacked graphene layers, and those assigned to Co_3O_4 NPs. In Figure 3b are presented the XRD pattern of Mn_3O_4 NPs and corresponding $\text{Mn}/\text{S}_3\text{N}_2\text{-GF}$ composite. In both patterns peaks can be observed at $2\theta \approx 18^\circ, 29^\circ, 31^\circ, 32^\circ, 36^\circ, 38^\circ, 44^\circ, 51^\circ, 54^\circ, 56^\circ, 58^\circ$ and 60° , indexed to (101), (112), (200), (103), (211), (004), (220), (105), (312), (303) and (321) XRD crystal planes of a body-centred-cubic phase/structure, respectively (ICDD PDF card no.04-004-864). The presence of these peaks confirms the existence of Mn_3O_4 NPs with spinel structure [39]. The XRD results validate the results obtained by Raman analysis confirming in situ preparation of metal oxide NPs in the presence of $\text{S}_3\text{N}_2\text{-GF}$. Additionally, the particle size of Co_3O_4 and Mn_3O_4 nanoparticles (pristine and in the presence of $\text{S}_3\text{N}_2\text{-GF}$) was estimated using Scherrer equation [40]. The Scherrer equation was used on the most prominent peak ($2\theta = 27^\circ$ for Co_3O_4 and $\text{Co}/\text{S}_3\text{N}_2\text{-GF}$, $2\theta = 36^\circ$ for Mn_3O_4 and $2\theta = 29^\circ$ for $\text{Mn}/\text{S}_3\text{N}_2\text{-GF}$) leading to estimated particle size of 23.0, 13.1, 26.2 and 28.6 nm for Co_3O_4 , $\text{Co}/\text{S}_3\text{N}_2\text{-GF}$, Mn_3O_4 and $\text{Mn}/\text{S}_3\text{N}_2\text{-GF}$, respectively.

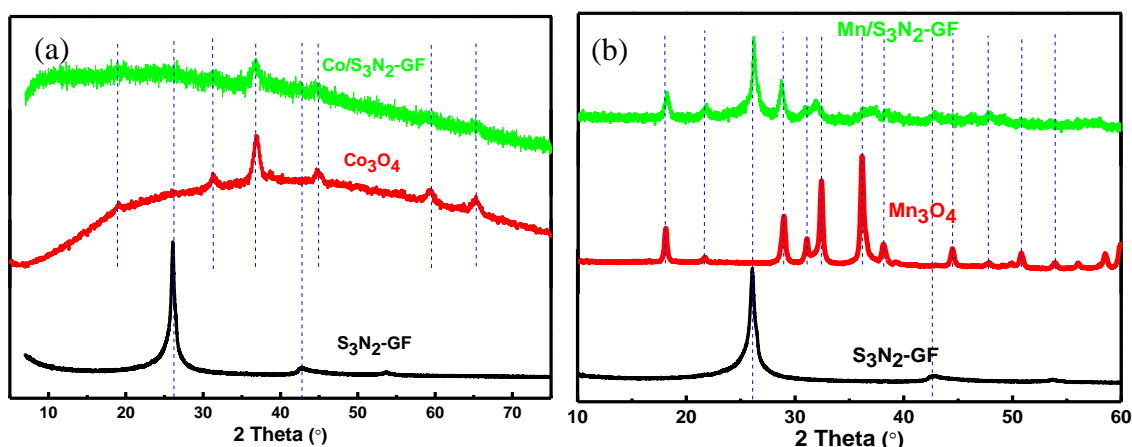


Figure 3. X-ray diffraction spectra of $\text{Co}/\text{S}_3\text{N}_2\text{-GF}$ (a) and $\text{Mn}/\text{S}_3\text{N}_2\text{-GF}$ (b) and the individual elements ($\text{S}_3\text{N}_2\text{-GF}$ and metal oxide NPs).

The morphology of $\text{S}_3\text{N}_2\text{-GF}$ and of both composites ($\text{Mn}/\text{S}_3\text{N}_2\text{-GF}$ and $\text{Co}/\text{S}_3\text{N}_2\text{-GF}$) was evaluated using TEM (Figure 4). The TEM image of $\text{S}_3\text{N}_2\text{-GF}$ (Figure 4a) shows graphene sheets which appear transparent and clear, consistent with literature reports [41,42]. The TEM image of $\text{Co}/\text{S}_3\text{N}_2\text{-GF}$ suggests that spherical Co_3O_4 nanoparticles, which have been formed, agglomerate onto the surface of $\text{S}_3\text{N}_2\text{-GF}$ sheets (Figure 4b). For the $\text{Mn}/\text{S}_3\text{N}_2\text{-GF}$ composite, the TEM images show a section with dispersed tetragonal-shaped Mn_3O_4 NPs on the surface of $\text{S}_3\text{N}_2\text{-GF}$ and another with some agglomeration (Figure 4c). It can also be seen on the TEM micrographs that the Mn_3O_4 nanoparticles formed comparably larger particles on the surface of $\text{S}_3\text{N}_2\text{-GF}$ sheets when compared with the Co_3O_4 nanoparticles. The energy dispersive spectroscopy (EDS) analysis also suggests the presence of Mn_3O_4 and Co_3O_4 , through the observation of Mn and Co species on the spectra. The presence of Cu on the spectra arises from the copper grids used as support during TEM analysis.

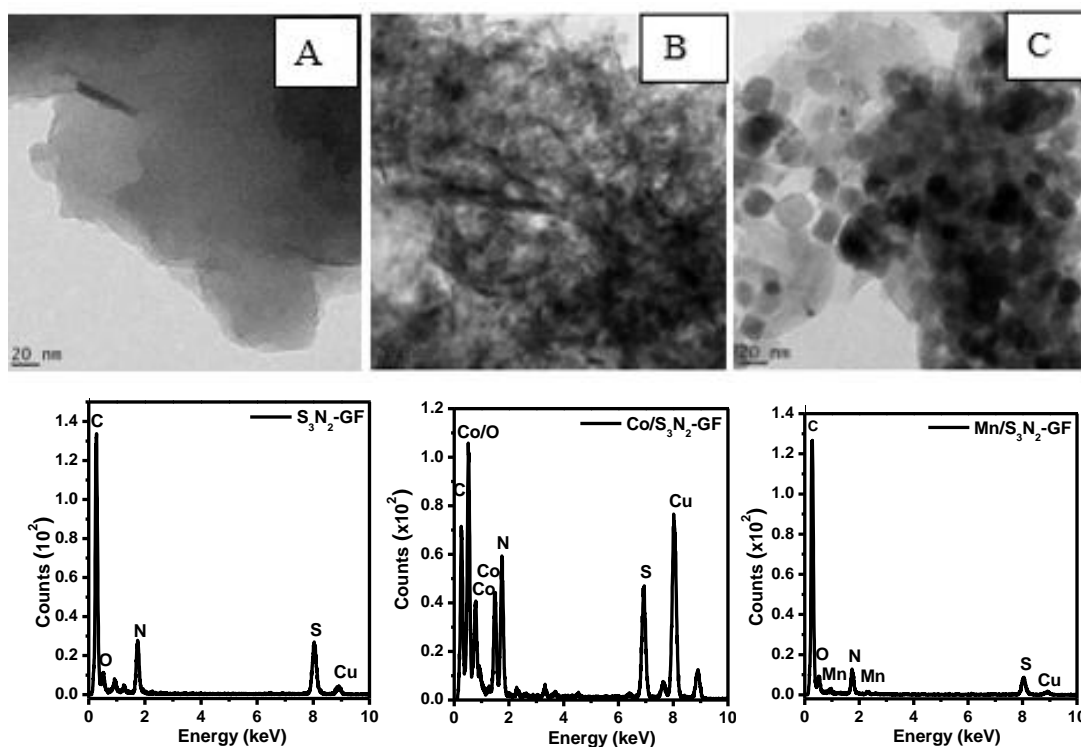


Figure 4. Transmission electron micrographs of S₃N₂-GF (A), Co/S₃N₂-GF (B) and Mn/S₃N₂-GF (C) with their corresponding EDS spectra.

3.2. Electrochemical Performance of the Electrocatalysts towards ORR

The three materials prepared (S₃N₂-GF, Co/S₃N₂-GF and Mn/S₃N₂-GF) were evaluated as ORR electrocatalysts using cyclic voltammetry (CV) in nitrogen- and oxygen-saturated solutions (0.1 mol dm⁻³ KOH). The CVs can be observed in Figure 5. In the absence of oxygen, no electrochemical processes are observed for S₃N₂-GF and Co/S₃N₂-GF, whereas for Mn/S₃N₂-GF a redox pair with very low intensity can be observed ($E_{pc} = 0.85$ V and $E_{pa} = 1.07$ V vs. RHE). This pair of peaks can be attributed to manganese redox processes [21,43]. On the other hand, when oxygen is present, all composites show an irreversible ORR peak at $E_{pc} = 0.63$, 0.76 and 0.80 V vs. RHE for S₃N₂-GF, Co/S₃N₂-GF and Mn/S₃N₂-GF, respectively. In the same experimental conditions, for Pt/C (20 wt. %) the ORR peak was observed at $E_{pc} = 0.86$ V vs. RHE.

All composites were further studied by linear sweep voltammetry (LSV) in 0.1 mol dm⁻³ KOH in both N₂- and O₂-saturated solutions. Figure 6a shows the LSV for Pt/C, S₃N₂-GF, Co/S₃N₂-GF and Mn/S₃N₂-GF in O₂-saturated solution (after the subtraction of LSV in N₂-saturated solution) and the main parameters determined are in Table 1. It can be clearly seen that the introduction of cobalt and manganese oxide nanoparticles into the S, N-doped GF leads to an improvement of the ORR features, not only in terms of diffusion-limiting current density (j_L) values, but also onset potentials. The first duplicates from S₃N₂-GF (−2.05 mA cm⁻²) to Co/S₃N₂-GF and Mn/S₃N₂-GF (−4.50 and −3.66 mA cm⁻², respectively), while the E_{onset} values shift 140 and 120 mV, respectively, towards more positive potentials. The onset potentials of both composites are similar to the value obtained for Pt/C and Co/S₃N₂-GF present comparable j_L value to that obtained for Pt/C. However, Mn/S₃N₂-GF shows a lower j_L value than Pt/C (less 20%). As evidenced by LSV results, Co/S₃N₂-GF displays the highest ORR activity among the three composites prepared, which is reflected by its having the most positive E_{onset} and highest j_L value.

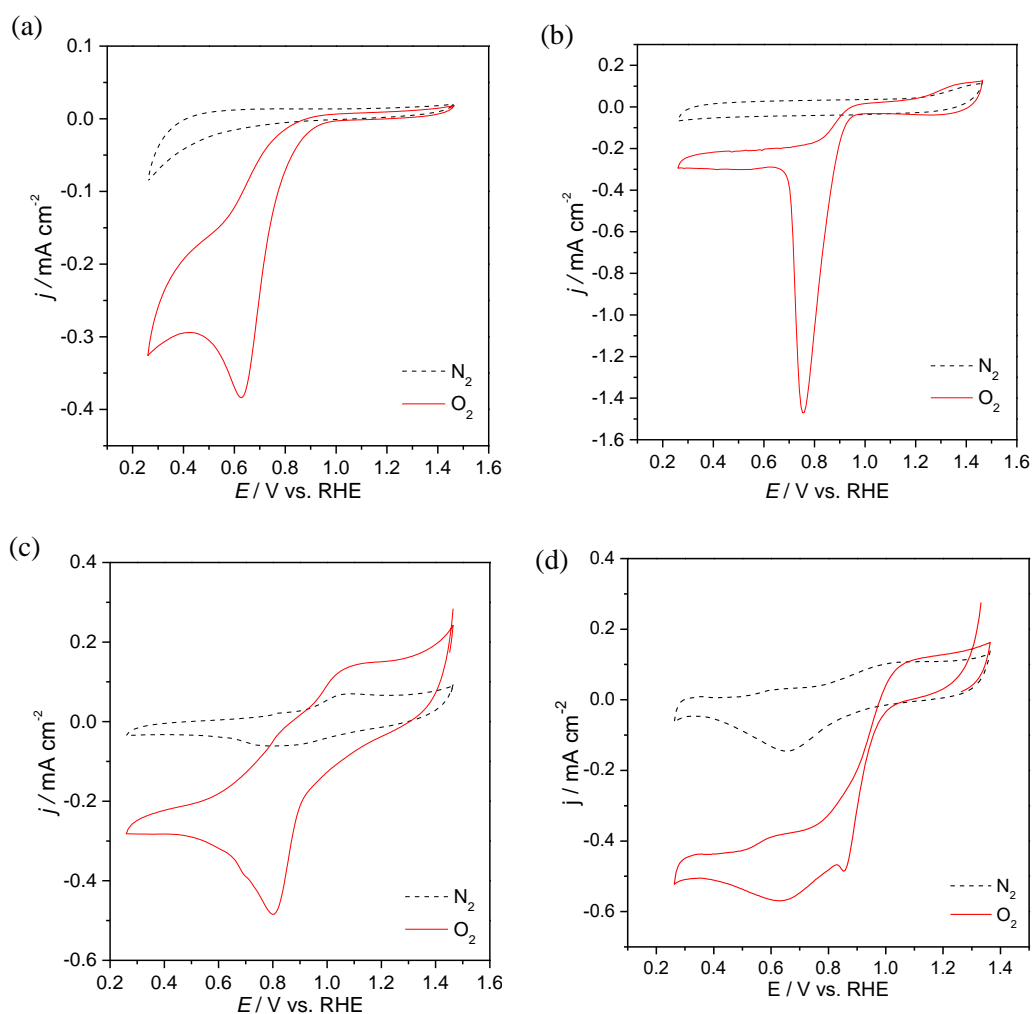


Figure 5. CVs in N_2 -saturated (dash line) and O_2 -saturated (full line) 0.1 mol dm^{-3} KOH solution at 0.005 V s^{-1} for $\text{S}_3\text{N}_2\text{-GF}$ (a), $\text{Co/S}_3\text{N}_2\text{-GF}$ (b), $\text{Mn/S}_3\text{N}_2\text{-GF}$ (c) and commercial Pt/C (20wt%) modified electrodes (d).

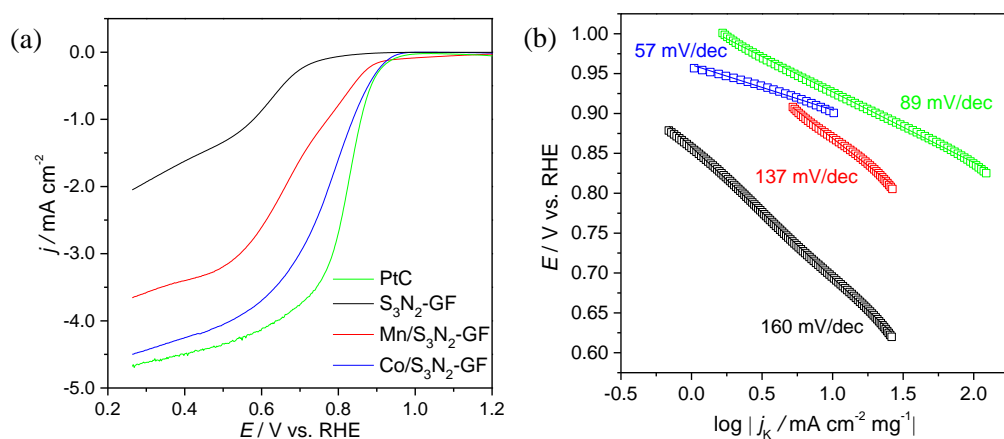


Figure 6. ORR LSV curves obtained in 0.1 mol dm^{-3} KOH saturated with O_2 for Pt/C, $\text{S}_3\text{N}_2\text{-GF}$, $\text{Co/S}_3\text{N}_2\text{-GF}$ and $\text{Mn/S}_3\text{N}_2\text{-GF}$ at 1600 rpm and 0.005 V s^{-1} (a) and the corresponding ORR Tafel plots (b).

Table 1. Onset potentials (E_{onset}), diffusion-limiting current density values ($j_{L,0.26 \text{ V},1600 \text{ rpm}}$) and Tafel slopes determined from the ORR LSV curves in 0.1 mol dm^{-3} KOH and the number of electrons transferred for each O_2 molecule.

Sample	E_{onset} (5% Total)	E_{onset} ($j = 0.1 \text{ mA cm}^{-2}$)	j_L (mA cm^{-2})	Tafel (mV dec^{-1})	\bar{n}_{O_2}
Pt/C	0.91	0.94	−4.67	89	4.0
$\text{S}_3\text{N}_2\text{-GF}$	0.77	0.77	−2.05	164	3.6
$\text{Co/S}_3\text{N}_2\text{-GF}$	0.91	0.93	−4.50	57	4.1
$\text{Mn/S}_3\text{N}_2\text{-GF}$	0.89	0.89	−3.66	137	3.9

LSVs at different rotation speeds and quantitative Koutecky–Levich (KL) plots were obtained to gather more information about the ORR kinetics of these composites. Figure 7 shows the LSV in O_2 -saturated solution (after the subtraction of LSV in N_2 -saturated solution) while the corresponding KL plots can be observed in Figure 8. Both the composites prepared and Pt/C electrocatalyst show a first order ORR in relation to the concentration of oxygen dissolved with the KL plots presenting good linearity with lines showing similar slopes in the potential range scanned for each material. This suggests that the applied potential does not have a significant influence on the number of electrons transferred per oxygen molecule (n_{O_2}). In fact, the n_{O_2} values estimated were almost constant with $n_{\text{O}_2} = 4.0, 3.6, 4.1$ and 3.9 for Pt/C, $\text{S}_3\text{N}_2\text{-GF}$, $\text{Co/S}_3\text{N}_2\text{-GF}$ and $\text{Mn/S}_3\text{N}_2\text{-GF}$, respectively. These values show that the ORR process at these electrocatalysts seems to proceed via a direct pathway (direct reduction of oxygen to water) involving four electrons. In the fuel cell industry, this is the preferred pathway, since it directly produces OH^- ions as the final product without the formation of OOH^- ions.

The results obtained for the $\text{Co/S}_3\text{N}_2\text{-GF}$ and $\text{Mn/S}_3\text{N}_2\text{-GF}$ composites are similar or better than others reported for similar compounds. For example, Duan et al. reported the application of Mn_3O_4 nanoparticles on nitrogen-doped graphene ($\text{Mn}_3\text{O}_4\text{@N-GF}$) [43] and on N-doped reduced graphene oxide ($\text{Mn}_3\text{O}_4\text{/N-rGO}$) [44] as ORR electrocatalysts with $0.87 \geq E_{\text{onset}} \geq 0.83 \text{ V}$ and $n_{\text{O}_2} = 3.8$. Wang and co-workers have also successfully applied a $\text{Co}_3\text{O}_4\text{@g-C}_3\text{N}_4\text{/NG}$ electrocatalyst for ORR, reaching an n_{O_2} of 3.9 and a j_L of -5.0 mA cm^{-2} ; however, the preparation of the electrocatalysts was time consuming and involved harsh conditions (higher temperatures) [10].

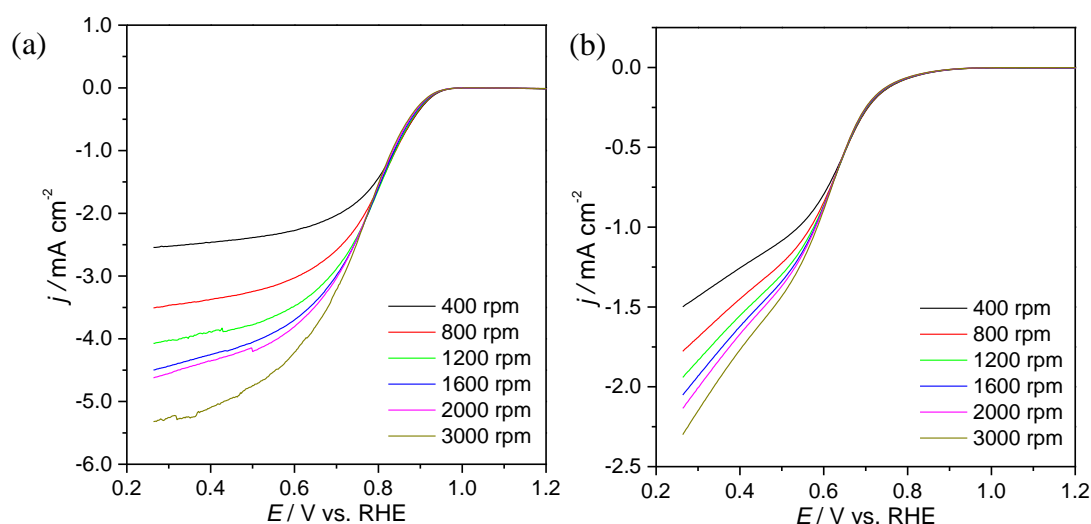


Figure 7. Cont.

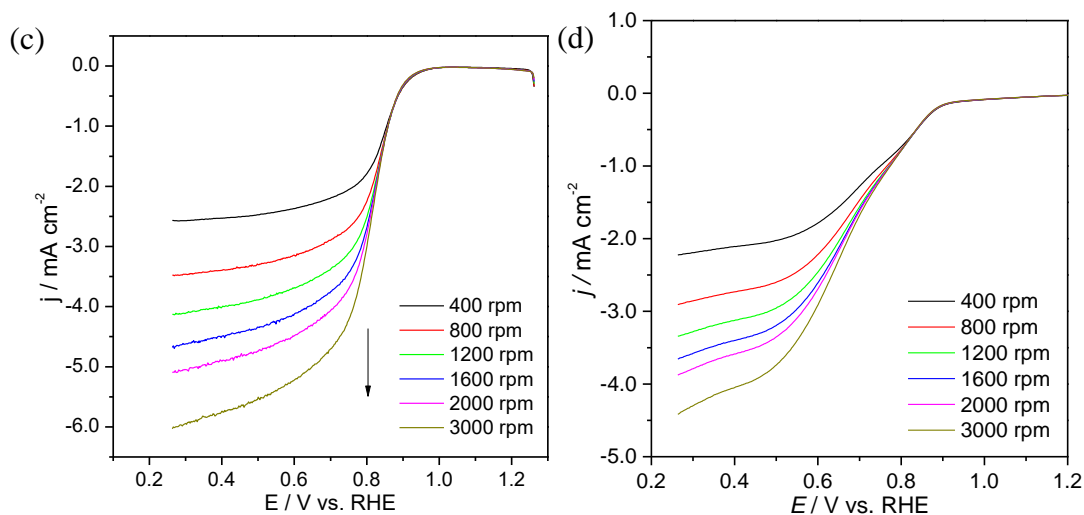


Figure 7. ORR polarization curves at different rotation rates in O_2 -saturated 0.1 mol dm^{-3} KOH solution at 0.005 V s^{-1} for $\text{S}_3\text{N}_2\text{-GF}$ (a), $\text{Co/S}_3\text{N}_2\text{-GF}$ (b), $\text{Mn/S}_3\text{N}_2\text{-GF}$ (c) and commercial Pt/C (20wt%) modified electrodes (d).

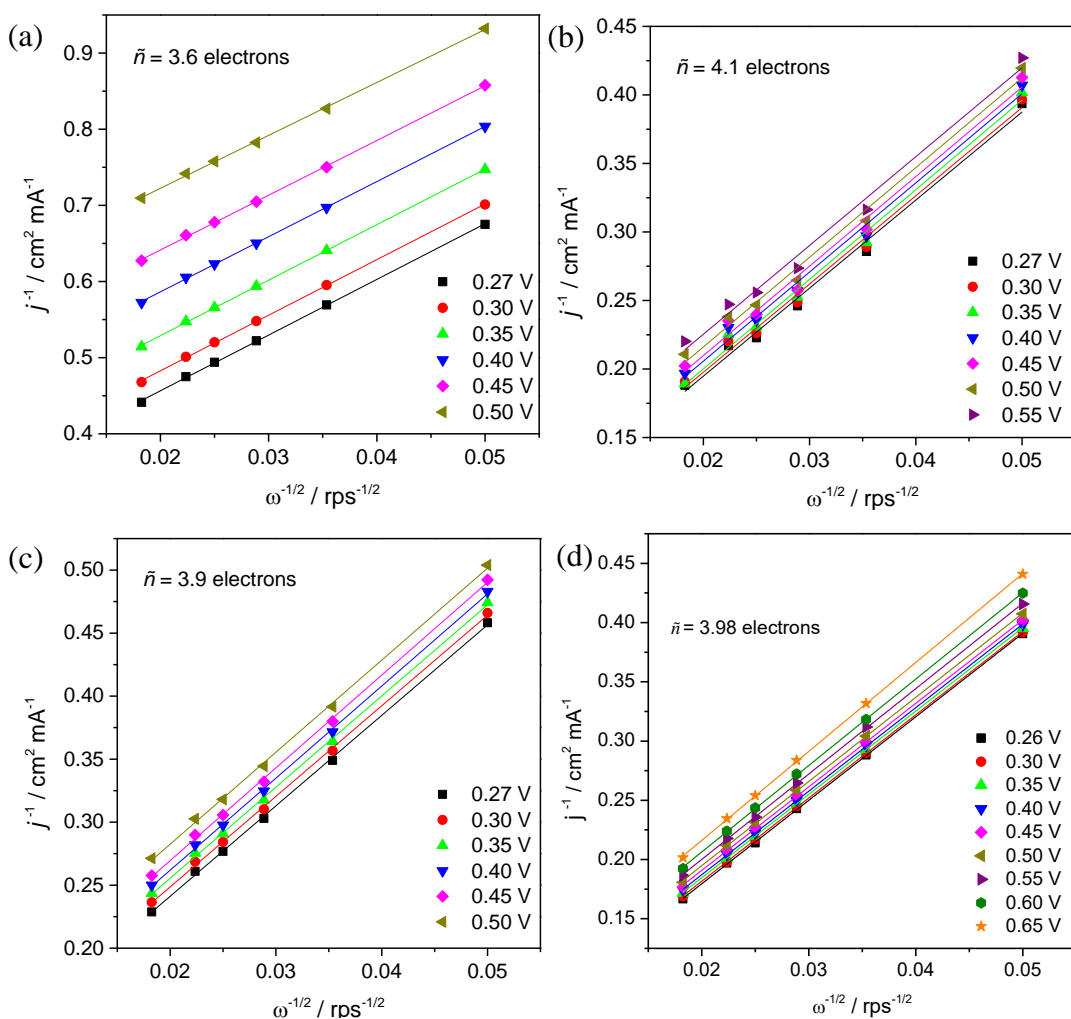


Figure 8. Koutecky–Levich (KL) plots obtained from the data in Figure 7 for $\text{S}_3\text{N}_2\text{-GF}$ (a), $\text{Co/S}_3\text{N}_2\text{-GF}$ (b), $\text{Mn/S}_3\text{N}_2\text{-GF}$ (c) and commercial Pt/C (20wt%)-modified electrodes (d).

The excellent ORR performance of the as-prepared composites can be attributed to nitrogen and sulphur dual-doping, introduced asymmetry charge and spin density, and strong coupling between Co_3O_4 or Mn_3O_4 nanoparticles and doped graphene flakes. The unbalanced charge distribution resulting from nitrogen and sulphur dual-doping is considerably favourable to oxygen adsorption, while a strong bonding between doped graphene flakes and Co_3O_4 or Mn_3O_4 nanoparticles (NPs) can facilitate the electron transfer, and also assures a good durability.

Tafel plots were obtained from the LSV curves at 1600 rpm and are depicted in Figure 6b. The Pt/C electrocatalysts presents an ORR Tafel slope of 89 mV dec^{-1} while for $\text{S}_3\text{N}_2\text{-GF}$, $\text{Co/S}_3\text{N}_2\text{-GF}$ and $\text{Mn/S}_3\text{N}_2\text{-GF}$ composites the values obtained were 160, 57 and 137 mV dec^{-1} . These results suggest that for $\text{Co/S}_3\text{N}_2\text{-GF}$ the global reaction rate is ruled by the conversion of intermediate surface adsorbed specie MOO- to MOOH with M representing an empty site on the surface of EC. For $\text{S}_3\text{N}_2\text{-GF}$ and $\text{Mn/S}_3\text{N}_2\text{-GF}$ the rate is defined by the consumption of MOOH species or by the first discharge step [45]. Additionally, the fact that the $\text{Co/S}_3\text{N}_2\text{-GF}$ composite presents a lower Tafel slope than Pt/C suggests that it can easily adsorb oxygen molecules onto its surface and activate it, boosting the ORR electrocatalytic performance.

The application of electrocatalysts as cathodes in fuel cells powered by methanol is highly dependent on their tolerance to methanol crossover. The evaluation of potential electrocatalysts' methanol tolerance is of extreme importance since in this type of fuel cells, the fuel (methanol) can permeate from the anode to the cathode through the polymer membrane. This will cause a critical decay in the EC performance as the active sites will be used for methanol oxidation contributing to a progressive CO poisoning leading to a continuous decrease in active sites for ORR. To evaluate the methanol crossover effect, a chronoamperometric test was performed in 0.1 mol dm^{-3} KOH saturated with O_2 and the results are presented in Figure 9a.

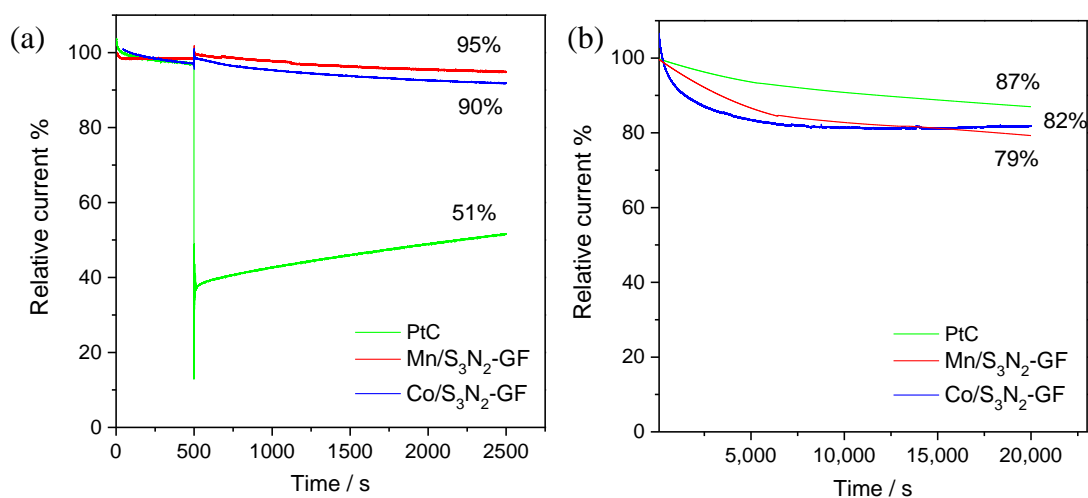


Figure 9. Chronoamperometric responses at $E = 0.50 \text{ V}$ vs. RHE and 1600 rpm of Pt/C, $\text{Co/S}_3\text{N}_2\text{-GF}$ and $\text{Mn/S}_3\text{N}_2\text{-GF}$ in 0.1 mol dm^{-3} O_2 -saturated KOH with the addition of 0.5 mol dm^{-3} methanol at $t = 500 \text{ s}$ (a) and without any addition for 20,000 s (b).

The addition of methanol causes a current decrease of $\approx 49\%$ when Pt/C is used; however, for $\text{Co/S}_3\text{N}_2\text{-GF}$ and $\text{Mn/S}_3\text{N}_2\text{-GF}$, its influence is almost insignificant, leading to current retentions of 90% and 95%, respectively. These results suggest a greater selectivity of the prepared composites towards ORR compared to methanol oxidation which constitutes a huge advantage when developing electrocatalysts for direct methanol fuel cells.

Another crucial issue when developing ORR electrocatalysts is their durability. In order to evaluate the $\text{Co/S}_3\text{N}_2\text{-GF}$ and $\text{Mn/S}_3\text{N}_2\text{-GF}$ stability, a chronoamperometric test was performed for 20,000 s in O_2 -saturated KOH at 0.50 V and 1600 rpm. Figure 9b shows the obtained results (Pt/C was included for comparison) and it can be seen even though Pt/C shows higher stability (87% current

retention), the prepared electrocatalysts present very similar values of current retention (79% and 82%) suggesting good stability.

4. Conclusions

The synthesis of metal oxide (Mn_3O_4 and Co_3O_4) impregnated the S_3N_2 -GF electrocatalyst with enhanced electrochemical properties towards ORR is here reported using a simple, scalable and cost-effective method. The structural characterization of the materials showed the preservation of the Mn_3O_4 and Co_3O_4 spinel structures. All prepared nanocomposites displayed superior overall ORR electrocatalytic activity in the alkaline medium with $\text{Co}/\text{S}_3\text{N}_2$ -GF and $\text{Mn}/\text{S}_3\text{N}_2$ -GF presenting the most promising results, with E_{onset} values of 0.91 and 0.89 V vs. RHE and j_L values of -4.50 and -3.66 mA cm^{-2} , respectively. The improved performance of metal oxide-containing composites was attributed to the coupling between Co_3O_4 or Mn_3O_4 nanoparticles and nitrogen and sulphur dual-doped graphene flakes. Furthermore, these two composites revealed an excellent tolerance to methanol and good stability. This work contributed to an efficient, simple, scalable and low-cost procedure for the development of efficient and naturally abundant ORR electrocatalysts.

Supplementary Materials: The following are available online at <http://www.mdpi.com/1996-1944/13/7/1562/s1>, Figure S1 shows the deconvoluted high resolution XPS spectra of S_3N_2 -GF: C 1s (a), O 1s (b), N 1s (c) and S 2p (d) and Figure S2 shows the full FTIR spectra.

Author Contributions: The synthesis and characterization of composite materials was performed by P.M. and E.I.I. helped in the analysis of data. The electrocatalytic experiments were conducted by P.M., D.M.F. and R.M. contributed to experiments involving methanol crossover and stability. D.M.F. and C.F. supervised the research and D.M.F. and P.M. were responsible for writing of the manuscript. All authors have read and agreed to the published version of the manuscript.

Funding: This work was financially supported by: Project UNIRCELL - POCI-01-0145-FEDER-16422 – funded by European Structural and Investment Funds (FEEL) through - Programa operacional Competitividade e Internacionalização - COMPETE2020 and by national funds through FCT - Fundação para a Ciência e a Tecnologia, I.P. Acknowledgments are also due to the FCT - project UID/QUI/50006/2013-POCI/01/0145/FEDER/007265 and PTDC/QUI-ELT/28299/2017 (FOAM4NER). The stay of P. Mathumba at REQUIMTE/LAQV (Porto) was financially supported by Erasmus Mundus (AESOP+) European Commission Scholarship.

Conflicts of Interest: The authors declare no conflict of interest.

References

1. Stacy, J.; Regmi, Y.N.; Leonard, B.; Fan, M.H. The recent progress and future of oxygen reduction reaction catalysis: A review. *Renew. Sustain. Energy Rev.* **2017**, *69*, 401–414. [[CrossRef](#)]
2. Ren, X.F.; Lv, Q.Y.; Liu, L.F.; Liu, B.H.; Wang, Y.R.; Liu, A.M.; Wu, G. Current progress of Pt and Pt-based electrocatalysts used for fuel cells. *Sustain. Energy Fuels* **2020**, *4*, 15–30. [[CrossRef](#)]
3. Wu, D.Z.; Shen, X.C.; Pan, Y.B.; Yao, L.B.; Peng, Z.M. Platinum Alloy Catalysts for Oxygen Reduction Reaction: Advances, Challenges and Perspectives. *ChemNanoMat* **2020**, *6*, 32–41. [[CrossRef](#)]
4. Bezerra, C.W.B.; Zhang, L.; Lee, K.C.; Liu, H.S.; Marques, A.L.B.; Marques, E.P.; Wang, H.J.; Zhang, J.J. A review of Fe-N/C and Co-N/C catalysts for the oxygen reduction reaction. *Electrochim. Acta* **2008**, *53*, 4937–4951. [[CrossRef](#)]
5. Surya, K.; Michael, M.S.; Prabakaran, S.R.S. A review on advancement in non-noble metal based oxides as bifunctional catalysts for rechargeable non-aqueous Li/air battery. *Solid State Ion.* **2018**, *317*, 89–96. [[CrossRef](#)]
6. Chen, Z.W.; Higgins, D.; Yu, A.P.; Zhang, L.; Zhang, J.J. A review on non-precious metal electrocatalysts for PEM fuel cells. *Energy Environ. Sci.* **2011**, *4*, 3167–3192. [[CrossRef](#)]
7. Wu, G.; Zelenay, P. Nanostructured Nonprecious Metal Catalysts for Oxygen Reduction Reaction. *Accounts Chem. Res.* **2013**, *46*, 1878–1889. [[CrossRef](#)]
8. Cao, R.; Lee, J.S.; Liu, M.L.; Cho, J. Recent Progress in Non-Precious Catalysts for Metal-air Batteries. *Adv. Energy Mater.* **2012**, *2*, 816–829. [[CrossRef](#)]
9. Osgood, H.; Devaguptapu, S.V.; Xu, H.; Cho, J.; Wu, G. Transition metal (Fe, Co, Ni, and Mn) oxides for oxygen reduction and evolution bifunctional catalysts in alkaline media. *Nano Today* **2016**, *11*, 601–625. [[CrossRef](#)]

10. Wang, Y.Q.; Yin, X.; Shen, H.B.; Jiang, H.; Yu, J.W.; Zhang, Y.F.; Li, D.W.; Li, W.Z.; Li, J. Co_3O_4 @g- C_3N_4 supported on N-doped graphene as effective electrocatalyst for oxygen reduction reaction. *Int. J. Hydrog. Energy* **2018**, *43*, 20687–20695. [[CrossRef](#)]
11. Liang, Y.Y.; Li, Y.G.; Wang, H.L.; Zhou, J.G.; Wang, J.; Regier, T.; Dai, H.J. Co_3O_4 nanocrystals on graphene as a synergistic catalyst for oxygen reduction reaction. *Nat. Mater.* **2011**, *10*, 780–786. [[CrossRef](#)] [[PubMed](#)]
12. Wang, Q.; Hu, W.H.; Huang, Y.M. Nitrogen doped graphene anchored cobalt oxides efficiently bi-functionally catalyze both oxygen reduction reaction and oxygen evolution reaction. *Int. J. Hydrog. Energy* **2017**, *42*, 5899–5907. [[CrossRef](#)]
13. Kim, M.; Nam, D.H.; Park, H.Y.; Kwon, C.; Eom, K.; Yoo, S.; Jang, J.; Kim, H.J.; Cho, E.; Kwon, H. Cobalt-carbon nanofibers as an efficient support-free catalyst for oxygen reduction reaction with a systematic study of active site formation. *J. Mater. Chem. A* **2015**, *3*, 14284–14290. [[CrossRef](#)]
14. Gebremariam, T.T.; Chen, F.Y.; Wang, Q.; Wang, J.L.; Liu, Y.X.; Wang, X.L.; Qaseem, A. Bimetallic Mn-Co Oxide Nanoparticles Anchored on Carbon Nanofibers Wrapped in Nitrogen-Doped Carbon for Application in Zn-Air Batteries and Supercapacitors. *ACS Appl. Energy Mater.* **2018**, *1*, 1612–1625. [[CrossRef](#)]
15. Sun, M.; Liu, H.; Liu, Y.; Qu, J.; Li, J. Graphene-based transition metal oxide nanocomposites for the oxygen reduction reaction. *Nanoscale* **2015**, *7*, 1250–1269. [[CrossRef](#)]
16. Zhou, R.; Jaroniec, M.; Qiao, S.Z. Nitrogen-doped carbon electrocatalysts decorated with transition metals for the oxygen reduction reaction. *ChemCatChem* **2015**, *7*, 3808–3817. [[CrossRef](#)]
17. Huang, Z.G.; Wang, J.; Peng, Y.; Jung, C.Y.; Fisher, A.; Wang, X. Design of Efficient Bifunctional Oxygen Reduction/Evolution Electrocatalyst: Recent Advances and Perspectives. *Adv. Energy Mater.* **2017**, *7*, 1700544. [[CrossRef](#)]
18. Fernandes, D.M.; Novais, H.C.; Bacsa, R.; Serp, P.; Bachiller-Baeza, B.; Rodriguez-Ramos, I.; Guerrero-Ruiz, A.; Freire, C. Polyoxotungstate@Carbon Nanocomposites As Oxygen Reduction Reaction (ORR) Electrocatalysts. *Langmuir* **2018**, *34*, 6376–6387. [[CrossRef](#)]
19. Mondal, T.K.; Dinda, D.; Saha, S.K. Nitrogen, sulphur co-doped graphene quantum dot: An excellent sensor for nitroexplosives. *Sens. Actuator B-Chem.* **2018**, *257*, 586–593. [[CrossRef](#)]
20. Lipinska, M.E.; Rebelo, S.L.H.; Pereira, M.F.R.; Gomes, J.; Freire, C.; Figueiredo, J.L. New insights into the functionalization of multi-walled carbon nanotubes with aniline derivatives. *Carbon* **2012**, *50*, 3280–3294. [[CrossRef](#)]
21. Fernandes, D.M.; Mathumba, P.; Fernandes, A.J.S.; Iwuoha, E.I.; Freire, C. Towards efficient oxygen reduction reaction electrocatalysts through graphene doping. *Electrochim. Acta* **2019**, *319*, 72–81. [[CrossRef](#)]
22. Sheng, Z.H.; Shao, L.; Chen, J.J.; Bao, W.J.; Wang, F.B.; Xia, X.H. Catalyst-Free Synthesis of Nitrogen-Doped Graphene via Thermal Annealing Graphite Oxide with Melamine and Its Excellent Electrocatalysis. *ACS Nano* **2011**, *5*, 4350–4358. [[CrossRef](#)] [[PubMed](#)]
23. Jarrais, B.; Guedes, A.; Freire, C. Heteroatom-Doped Carbon Nanomaterials as Metal-Free Catalysts for the Reduction of 4-Nitrophenol. *ChemistrySelect* **2018**, *3*, 1737–1748. [[CrossRef](#)]
24. Guo, Y.P.; Zeng, Z.Q.; Li, Y.L.; Huang, Z.G.; Cui, Y. In-situ sulfur-doped carbon as a metal-free catalyst for persulfate activated oxidation of aqueous organics. *Catal. Today* **2018**, *307*, 12–19. [[CrossRef](#)]
25. Bhagade, S.S.; Chaurasia, S.R.; Bhanage, B.M. Reductive-hydroformylation of 1-octene to nonanol using fibrous Co_3O_4 catalyst. *Catal. Today* **2018**, *309*, 147–152. [[CrossRef](#)]
26. Uddin, M.K.; Baig, U. Synthesis of Co_3O_4 nanoparticles and their performance towards methyl orange dye removal: Characterisation, adsorption and response surface methodology. *J. Clean. Prod.* **2019**, *211*, 1141–1153. [[CrossRef](#)]
27. Swetha, J.V.; Parse, H.; Kakade, B.; Geetha, A. Morphology dependent facile synthesis of manganese oxide nanostructures for oxygen reduction reaction. *Solid State Ion.* **2018**, *328*, 1–7. [[CrossRef](#)]
28. Liu, X.J.; Zhou, W.J.; Yang, L.J.; Li, L.G.; Zhang, Z.Y.; Ke, Y.T.; Chen, S.W. Nitrogen and sulfur co-doped porous carbon derived from human hair as highly efficient metal-free electrocatalysts for hydrogen evolution reactions. *J. Mater. Chem. A* **2015**, *3*, 8840–8846. [[CrossRef](#)]
29. Zhou, J.H.; Yue, H.H.; Qi, F.; Wang, H.Q.; Chen, Y.F. Significantly enhanced electrocatalytic properties of three-dimensional graphene foam via Ar plasma pretreatment and N, S co-doping. *Int. J. Hydrog. Energy* **2017**, *42*, 27004–27012. [[CrossRef](#)]
30. Pisana, S.; Lazzeri, M.; Casiraghi, C.; Novoselov, K.S.; Geim, A.K.; Ferrari, A.C.; Mauri, F. Breakdown of the adiabatic Born-Oppenheimer approximation in graphene. *Nature Mater.* **2007**, *6*, 198–201. [[CrossRef](#)]

31. Song, X.Y.; Ma, X.L.; Ning, G.Q.; Gao, D.W.; Yu, Z.Q.; Xiao, Z.H. The orientation construction of S and N dual-doped discoid-like graphene with high-rate electrode property. *Appl. Surf. Sci.* **2018**, *442*, 467–475. [[CrossRef](#)]
32. Tian, P.F.; Zang, J.B.; Jia, S.P.; Zhang, Y.; Gao, H.W.; Zhou, S.Y.; Wang, W.P.; Xu, H.Q.; Wang, Y.H. Preparation of S/N co-doped graphene through a self-generated high gas pressure for high rate supercapacitor. *Appl. Surf. Sci.* **2018**, *456*, 781–788. [[CrossRef](#)]
33. Araujo, M.P.; Nunes, M.; Rocha, I.M.; Pereira, M.F.R.; Freire, C. Co₃O₄ Nanoparticles Anchored on Selectively Oxidized Graphene Flakes as Bifunctional Electrocatalysts for Oxygen Reactions. *ChemistrySelect* **2018**, *3*, 10064–10076. [[CrossRef](#)]
34. Ren, Q.M.; Feng, Z.T.; Mo, S.P.; Huang, C.L.; Li, S.J.; Zhang, W.X.; Chen, L.M.; Fu, M.L.; Wu, J.L.; Ye, D.Q. 1D-Co₃O₄, 2D-Co₃O₄, 3D-Co₃O₄ for catalytic oxidation of toluene. *Catal. Today* **2019**, *332*, 160–167. [[CrossRef](#)]
35. Hassani, S.S.; Samiee, L.; Ghasemy, E.; Rashidi, A.; Ganjali, M.R.; Tasharofi, S. Porous nitrogen-doped graphene prepared through pyrolysis of ammonium acetate as an efficient ORR nanocatalyst. *Int. J. Hydrog. Energy* **2018**, *43*, 15941–15951. [[CrossRef](#)]
36. Cai, D.D.; Wang, C.S.; Shi, C.Y.; Tan, N. Facile synthesis of N and S co-doped graphene sheets as anode materials for high-performance lithium-ion batteries. *J. Alloy. Compd.* **2018**, *731*, 235–242. [[CrossRef](#)]
37. Qiu, D.F.; Bu, G.; Zhao, B.; Lin, Z.X.; Pu, L.; Pan, L.J.; Shi, Y. In Situ growth of mesoporous Co₃O₄ nanoparticles on graphene as a high-performance anode material for lithium-ion batteries. *Mater. Lett.* **2014**, *119*, 12–15. [[CrossRef](#)]
38. Liang, C.; Li, X.F.; Su, D.F.; Ma, Q.Y.; Mao, J.Y.; Chen, Z.R.; Wang, Y.; Yao, J.; Li, H.R. Magnetic nano-structured cobalt cobalt oxide/nitrogen-doped carbon material as an efficient catalyst for aerobic oxidation of p-cresols. *Mol. Catal.* **2018**, *453*, 121–131. [[CrossRef](#)]
39. Araujo, M.P.; Nunes, M.; Rocha, I.M.; Pereira, M.F.R.; Freire, C. Electrocatalytic activity of new Mn₃O₄@oxidized graphene flakes nanocomposites toward oxygen reduction reaction. *J. Mater. Sci.* **2019**, *54*, 8919–8940. [[CrossRef](#)]
40. Patterson, A.L. The Scherrer formula for X-ray particle size determination. *Phys. Rev.* **1939**, *56*, 978–982. [[CrossRef](#)]
41. Liu, X.; Jiang, L.X.; Zhu, Z.J.; Chen, S.; Dou, Y.H.; Liu, P.R.; Wang, Y.; Yin, H.J.; Tang, Z.Y.; Zhao, H.J. Wet-chemistry grafted active pyridinic nitrogen sites on holey graphene edges as high performance ORR electrocatalyst for Zn-Air batteries. *Mater. Today Energy* **2019**, *11*, 24–29. [[CrossRef](#)]
42. Xu, H.; Lin, Q.L.; Zhou, T.H.; Chen, T.T.; Lin, S.P.; Dong, S.H. Facile preparation of graphene nanosheets by pyrolysis of coal-tar pitch with the presence of aluminum. *J. Anal. Appl. Pyrolysis* **2014**, *110*, 481–485. [[CrossRef](#)]
43. Duan, J.J.; Zheng, Y.; Chen, S.; Tang, Y.H.; Jaroniec, M.; Qiao, S.Z. Mesoporous hybrid material composed of Mn₃O₄ nanoparticles on nitrogen-doped graphene for highly efficient oxygen reduction reaction. *Chem. Commun.* **2013**, *49*, 7705–7707. [[CrossRef](#)] [[PubMed](#)]
44. Duan, J.J.; Chen, S.; Dai, S.; Qiao, S.Z. Shape Control of Mn₃O₄ Nanoparticles on Nitrogen-Doped Graphene for Enhanced Oxygen Reduction Activity. *Adv. Funct. Mater.* **2014**, *24*, 2072–2078. [[CrossRef](#)]
45. Shinagawa, T.; Garcia-Esparza, A.T.; Takanebe, K. Insight on Tafel slopes from a microkinetic analysis of aqueous electrocatalysis for energy conversion. *Sci. Rep.* **2015**, *5*, 13801. [[CrossRef](#)]

